Light-Forbidden Transitions in Plasmon-Emitter Coupling

A. Cuartero-González[1] and A. I. Fernández-Domínguez[1,*]

[1]*Departamento de Física Teórica de la Materia Condensada and Condensed Matter Physics Center (IFIMAC), Universidad Autónoma de Madrid, E- 28049 Madrid, Spain*

We investigate the impact that light-forbidden exciton transitions have in the near-field population dynamics and far-field scattering spectrum of hybrid plasmon-emitter systems. Specifically, we consider a V-type quantum emitter, sustaining one dipolar and one quadrupolar (dipole-inactive) excited states, placed at the nanometric gap of a particle-on-a-mirror metallic cavity. Our fully analytical description of plasmon-exciton coupling for both exciton transitions enables us to reveal the conditions in which the presence of the latter greatly alters the Purcell enhancement and Rabi splitting phenomenology in the system.

The deeply sub-wavelength character of localized surface plasmons (SPs) provides new avenues for the control of light-matter interactions at the nanoscale, both in the weak [1, 2] and strong coupling regimes [3, 4]. Currently, hybrid systems comprising metal nanocavities and quantum emitters (QEs) are attracting much interest not only for their fundamental implications, but also for their technological prospects in areas such as photonics [5] and material science [6]. Lately, experimental reports have shown that the strong light confinement enabled by SPs can unveil features of microscopic light sources that remain hidden to propagating fields, such as mesoscopic effects in the electronic wavefunctions of quantum dots [7] or the fingerprint of individual chemical bonds in Raman molecules [8]. These advances indicate that in order to fully seize the potential of QE-SP devices their theoretical description [9] must combine the framework of macroscopic quantum electrodynamics, accounting for the lossy and open nature of SP quanta [10], and refined models for QEs, including ingredients such as rovibrational [11] or polarization degrees of freedom [12].

In this Letter, we investigate the impact that light-forbidden exciton transitions have in QE-SP interactions at the single emitter level. We consider a V-type three-level system with one dipolar and one quadrupolar (dipole-inactive) excited states. The latter are long-lived excitations which present radiative decay rates typically 5 orders of magnitude lower than dipolar ones [13, 14]. They are effectively decoupled from propagating light, but recent theoretical predictions [14–17] suggest that the large evanescent field gradients associated to SPs may allow Purcell enhancing these transitions up to time scales comparable to light-allowed ones. We explore the influence of this phenomenon in QE-SP coupling and the formation of plasmon-exciton-polaritons (PEPs) in an archetypal nanoparticle-on-a-mirror (NPoM) cavity [4]. Using transformation optics [18], we describe in a fully analytical manner the near- and far-field characteristics of the SP modes supported by this structure. This provides deep physical insights into the population dynamics and the scattering spectrum of the hybrid QE-SP system, and allows us to reveal the conditions in which light-forbidden excitons yield a strong modification of the Purcell enhancement and Rabi splitting phenomena.

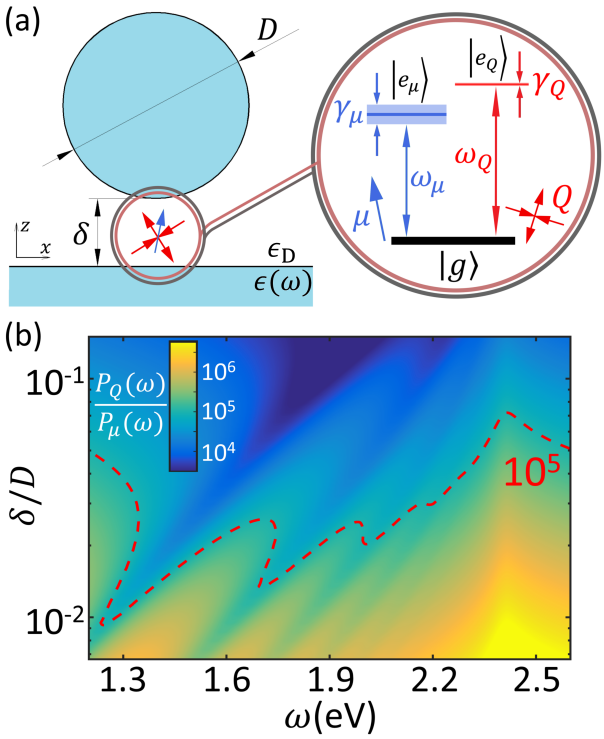

FIG. 1. (a) Sketch of the system under study: A QE is placed at the gap of a metallic NPoM cavity with $\delta = 0.9$ nm and $D = 30$ nm. The QE is modelled as a three-level system with one dipolar (μ) one quadrupolar (Q) excitonic transitions. (b) Ratio between the quadrupolar and dipolar Purcell factors evaluated at the gap center as a function of the exciton frequency and gap size.

Figure 1(a) sketches a NPoM cavity with diameter $D = 30$ nm and gap size $\delta = 0.9$ nm. The metal permittivity $\epsilon(\omega) = \epsilon_\infty - \omega_p^2/\omega(\omega - i\gamma)$ is a low-frequency Drude-fitting to Ag, see Supplemental Material (SM), and the whole structure is embedded in $\epsilon_D = 4$. A point-like three-level system is placed at $\mathbf{r}_{QE} = x_{QE}\hat{\mathbf{x}} + z_{QE}\hat{\mathbf{z}}$ (the coordinate origin is located at the bottom of the gap). The light-allowed transition has a dipole moment $\boldsymbol{\mu} = \mu\hat{\mathbf{z}}$, a natural frequency ω_μ, and radiative decay rate in vacuum $\gamma_\mu = \gamma_\mu(\omega_\mu) = \omega_\mu^3\mu^2/3\pi\epsilon_0\hbar c^3$. The light-forbidden one has a quadrupole moment $\boldsymbol{Q} = \frac{Q}{\sqrt{2}}[\hat{\mathbf{z}}\hat{\mathbf{x}} + \hat{\mathbf{x}}\hat{\mathbf{z}}]$, frequency

ω_Q and decay rate $\gamma_Q = \gamma_Q(\omega_Q) = \omega_Q^5 Q^2/360\pi\epsilon_0\hbar c^5$. Nonradiative decay in the QE is neglected, and the orientation of both excitonic moments is chosen to maximize SP coupling. We take $\mu = 0.56$ e·nm, $\omega_\mu = 1.55$ eV and $\gamma_\mu = 0.6$ μeV. These parameters and the NPoM dimensions are in accordance with the experimental set-up in Ref. [4].

Using transformation optics, we can calculate the scattering Green function, $\mathbf{G}(\mathbf{r}, \mathbf{r}_{\rm QE})$, for the cavity in Figure 1(a) [19]. In order to keep our calculations fully analytical for all system configurations, we model the near-field characteristics of the cavity geometry through its 2D counterpart [20] (which assumes translational symmetry along the y-direction). Note that recent reports indicate that the phenomenology of QE-SP strong coupling in 2D and 3D NPoMs is remarkaby similar [21]. Thus, the total Purcell factors for dipolar and quadrupolar transitions read [22]

$$\begin{aligned} P_\mu(\omega) &= \tfrac{8}{\mu^2}\mathrm{Im}\{\boldsymbol{\mu}\mathbf{G}(\mathbf{r},\mathbf{r}_{\rm QE})\boldsymbol{\mu}\}_{\mathbf{r}=\mathbf{r}_{\rm QE}}, \\ P_Q(\omega) &= \tfrac{16c^2}{\omega^2 Q^2}\mathrm{Im}\{(\mathbf{Q}\nabla)(\nabla'\mathbf{G}(\mathbf{r},\mathbf{r}'))\mathbf{Q}\}_{\mathbf{r},\mathbf{r}'=\mathbf{r}_{\rm QE}}. \end{aligned} \quad (1)$$

Figure 1(b) renders P_Q/P_μ versus frequency and gap size evaluated at the gap center. The red dashed line plots the contour $P_Q/P_\mu = 10^5$, and sets the parameter region for which the time scales for light-forbidden and light-allowed exciton dynamics become comparable. For $\delta/D = 0.03$, there exist two spectral windows fulfilling this condition: below the lowest-frequency, bright SP mode (ω_1), and at the dark plasmonic pseudomode ($\omega_{\rm PS} \simeq \omega_{\rm p}/\sqrt{\epsilon_\infty + \epsilon_{\rm D}}$), which emerges from the spectral overlapping of high-frequency, tightly confined SPs [19].

Figure 2 shows the spectral density, $J_i(\omega) = \frac{\gamma_i(\omega)}{2\pi}P_i(\omega)$, for dipolar ($i = \mu$) and quadrupolar ($i = Q$) excitonic transitions within the cavity in Figure 1(a) and $Q = 0.52$ e·nm^2. This value is chosen so that the spectral density at the PS is the same for both excitons at $z_{\rm QE} = \delta/2$, although $J_Q(\omega)$ decays much faster with decreasing frequency. By displacing the emitter position to $z_{\rm QE} = 7\delta/8$, both spectral densities increase. This enhancement is much higher in $J_Q(\omega)$, which is fully governed by the PS, and whose maximum is 20 times larger than $J_\mu(\omega_{\rm PS})$. The bottom panels display the spatial dependence of the dipolar (quadrupolar) spectral density evaluated at $\omega_1 = 1.55$ eV ($\omega_{\rm PS} = 2.40$ eV). $J_\mu(\omega_1)$ is large within the gap region and is uniformly distributed across it. On the contrary, $J_Q(\omega_{\rm PS})$ is tightly confined at all metal surfaces (see zooms in central panels).

Under the high-quality resonator approximation [23], the analytical expressions for the spectral densities can be reshaped into a sum of lorentzian terms of the form

$$J_i(\omega) = \sum_{n=1,\infty}^{\sigma=\pm1} \frac{(g_i^{n,\sigma})^2}{\pi} \frac{\gamma_{n,\sigma}/2}{(\omega-\omega_{n,\sigma})^2 + (\gamma_{n,\sigma}/2)^2}, \quad (2)$$

where again $i = \mu, Q$, n is the SP azimuthal order, and σ the parity (even/odd) with respect to the gap center. The SM shows the validity of Equation (2) for the spectra in Figure 2(a). It also presents analytical expressions for the

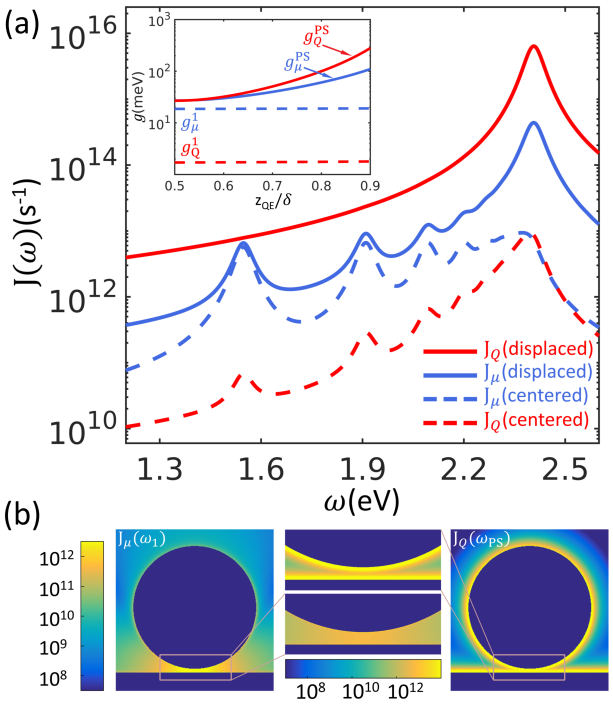

FIG. 2. (a) Spectral densities ($x_{\rm QE} = 0$, $\mu = 0.56$ e·nm, $Q = 0.52$ e·nm^2) evaluated at $z_{\rm QE} = \delta/2$ (dashed line) and $7\delta/8$ (solid line). Inset: Coupling strengths for the lowest-frequency SP (dashed) and the pseudomode (solid) as a function of $z_{\rm QE}$. (b) Spectral density maps for the dipolar (left) and quadrupolar (right) transitions at ω_1 and $\omega_{\rm PS}$, respectively. Central panels zoom at the gap region (note the difference in color scales).

SP frequencies $\omega_{n,\sigma}$ and decay rates $\gamma_{n,\sigma} = \gamma + \delta_{\sigma 1}\gamma_n^{\rm rad}$ (where γ is the Drude damping and $\gamma_n^{\rm rad}$ are the radiative rates of even SPs), as well as the QE-SP coupling constants $g_i^{n,\sigma}$. The inset of Figure 2(a) plots the coupling strengths for dipole and quadrupole excitons and for the lowest-frequency SP (the superscript $\sigma = 1$ is omitted) and for the pseudomode, $g_i^{\rm PS} = \sqrt{\sum_{n\geq 7,\sigma}(g_i^{n,\sigma})^2}$. Whereas the former do not depend on $z_{\rm QE}$, the latter grow exponentially as the QE approaches the metal surface, being this enhancement always larger for the quadrupole exciton.

We use our approach to assess the influence that light-forbidden transitions have in the exciton population dynamics. We assume that initially only the light-allowed state is populated ($n_\mu(0) = |c_\mu(0)|^2 = 1$ and $n_Q(0) = |c_Q(0)|^2 = 0$) and analyze how the excited state populations evolve in time. The Wigner-Weisskopf problem for our system consists in two coupled integro-differential equations of the form

$$\begin{aligned} \dot{c}_i(t) = &-\int_0^t d\tau c_i(\tau)\int_0^\infty J_i(\omega)e^{i(\omega-\omega_i)(\tau-t)}d\omega - \\ &-\int_0^t d\tau c_j(\tau)\int_0^\infty J_V(\omega)e^{i[(\omega-\omega_j)\tau-(\omega-\omega_i)t]}d\omega, \end{aligned} \quad (3)$$

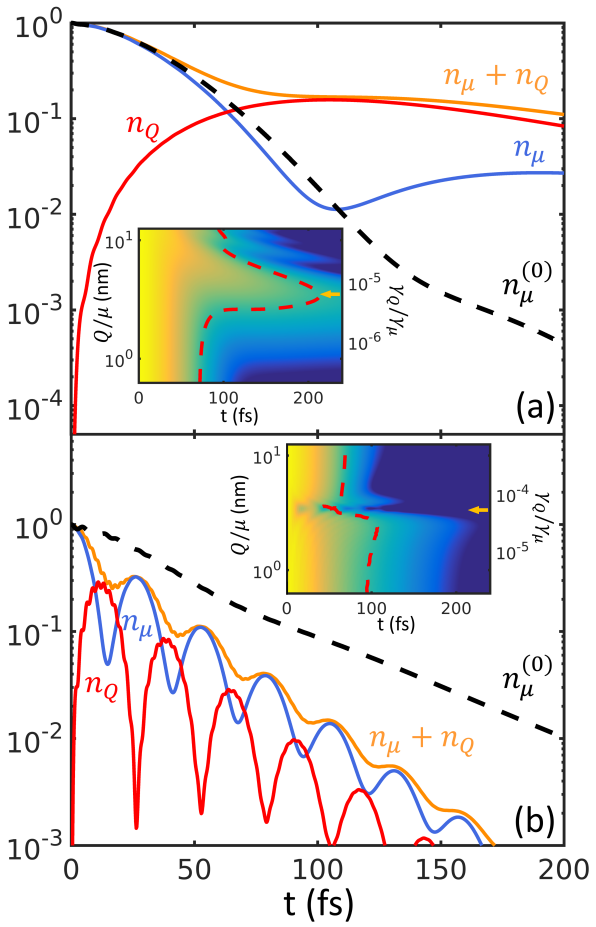

FIG. 3. Temporal evolution of the dipolar, n_μ, quadrupolar, n_Q, and total, $n_\mu + n_Q$, excitonic populations with initial condition $n_\mu(0) = 1$. For comparison, the dipole population in absence of the light-forbidden transition, $n_\mu^{(0)}$, is also shown. In panel (a), $\omega_\mu = \omega_Q = \omega_1$, $\gamma_Q/\gamma_\mu = 6 \cdot 10^{-6}$ and $z_{\rm QE} = \delta/2$. In panel (b), $\omega_\mu = \omega_1$, $\omega_Q = \omega_{\rm PS}$, $\gamma_Q/\gamma_\mu = 5 \cdot 10^{-5}$ and and $z_{\rm QE} = 7\delta/8$. Insets: total QE population dynamics as a function of γ_Q/γ_μ. Red dashed lines plot the contour $n_\mu + n_Q = 0.1$. Horizontal arrows indicate the cases considered in the main panels.

where $i, j = \mu, Q$ $(i \neq j)$, and $J_V(\omega)$ is given by Equation (2) with $g_V^{n,\sigma} = \sqrt{g_\mu^{n,\sigma} g_Q^{n,\sigma}}$. This spectral density feeds the second term in Equations (3), which couples the excitonic populations through the full plasmonic spectrum supported by the NPoM.

We investigate the population dynamics in two different configurations, already introduced in Figure 2. In Figure 3(a), the QE is placed at the gap center and the dipole and quadrupole transition frequencies are at resonance with the lowest SP mode, $\omega_Q = \omega_\mu = \omega_1$. In Figure 3(b), the QE is in the vicinity of the nanoparticle surface, $z_{\rm QE} = 7\delta/8$, and the quadrupole transition is shifted to the pseudomode frequency, $\omega_Q = \omega_{\rm PS}$. In the main panels, the population of the light-allowed, $n_\mu = |c_\mu|^2$ (blue), and light-forbidden, $n_Q = |c_Q|^2$ (red), states are shown, as well as the total QE population, $n_\mu + n_Q$ (orange). They are evaluated at $Q/\mu = 3.5$ nm, which corresponds to $\gamma_Q/\gamma_\mu = 6 \cdot 10^{-6}$ and $\gamma_Q/\gamma_\mu = 5 \cdot 10^{-5}$ in panels (a) and (b), respectively. For comparison, the dipole state populations in absence of the quadrupole exciton, $n_\mu^{(0)}$, are shown in black dashed lines. Note that both show a rather monotonic decay decorated by very shallow oscillations, which can be linked to the onset of the QE-SP strong coupling regime.

Figure 3(a) shows n_Q growing initially, up to crossing n_μ. At longer times, the quadrupole exciton feeds population back into the dipole state, and induces a decay in $n_\mu + n_Q$ which is significantly slower than $n_\mu^{(0)}$. The fingerprint of the quadrupole exciton is even more remarkable in Figure 3(b), where the fast Rabi oscillations in n_Q, which originate from its strong coupling to the PS, are transferred to n_μ as well. The resulting oscillating $n_\mu + n_Q$ profile decays much faster than $n_\mu^{(0)}$. Thus, we can conclude that depending on the configuration, light-forbidden transitions can effectively reduce or enlarge the QE lifetime, altering significantly the phenomenology of the Purcell effect in the system. The insets display $n_\mu + n_Q$ versus γ_Q/γ_μ and time, revealing that such strong modifications of QE lifetime due to light-forbidden excitons only take place within a certain range of Q-values in both configurations.

In order to evaluate the impact that the quadrupole exciton has in the performance of the QE-SP system as a photonic device, we study next its far-field scattering spectrum. We model a dark-field spectroscopy set-up [4] in which the NPoM is illuminated by a grazing laser field, $E_{\rm L}$, with frequency $\omega_{\rm L}$ and polarized along z-direction. Due to its inherent open and lossy nature, describing the scattering properties of the hybrid system would require, in principle, the computation of its steady-state density matrix out of a Liovillian formulation of the problem. However, in the limit of low pumping ($E_{\rm L} \to 0$), we can use a non-hermitian hamiltonian [24] of the form

$$\hat{H} = \sum_{n,\sigma} \tilde{\omega}_{n,\sigma} \hat{a}_{n,\sigma}^\dagger \hat{a}_{n,\sigma} + \tilde{\omega}_\mu \hat{\sigma}_\mu^\dagger \hat{\sigma}_\mu + \omega_Q \hat{\sigma}_Q^\dagger \hat{\sigma}_Q + \\ + \Big(\sum_{n,\sigma,j} g_j^{n,\sigma} \hat{a}_{n,\sigma}^\dagger \hat{\sigma}_j + E_{\rm L} e^{-i\omega_{\rm L} t} \hat{M}^\dagger + {\rm h.c.} \Big), \quad (4)$$

where $\hat{a}_{n,\sigma}^\dagger$ ($\hat{a}_{n,\sigma}$) and $\hat{\sigma}_j^\dagger$ ($\hat{\sigma}_j$) are the creation (annihilation) operators for SP and QE excitations, and $\tilde{\omega}_{n,\sigma} = \omega_{n,\sigma} - i\frac{\gamma_{n,\sigma}}{2}$ and $\tilde{\omega}_\mu = \omega_\mu - i\sqrt{\epsilon_{\rm D}}\frac{\gamma_\mu}{2}$ are the complex frequencies for the SPs and the QE dipole transition, respectively (note that the latter radiates in a dielectric background $\epsilon_{\rm D}$).

The Hamiltonian in Equation (4) is equivalent to the one behind Equations (2) except for the last term. This accounts for the coherent pumping of the system, with $\hat{M} = \sum_n \mu_n \hat{a}_{n,1} + \mu \hat{\sigma}_\mu$. Note that the SP dipole momenta can be obtained (see SM) from the radiative decay rates as $\mu_n = \frac{\epsilon(\omega_{n,1}) - \epsilon_{\rm D}}{2\epsilon(\omega_{n,1})} \sqrt{3\pi\epsilon_0 \hbar \gamma_n^{\rm rad} c^3 / \sqrt{\epsilon_{\rm D}} \omega_{n,1}^3}$. We solve the Schrödinger equation for $\hat{H}$ transformed into the

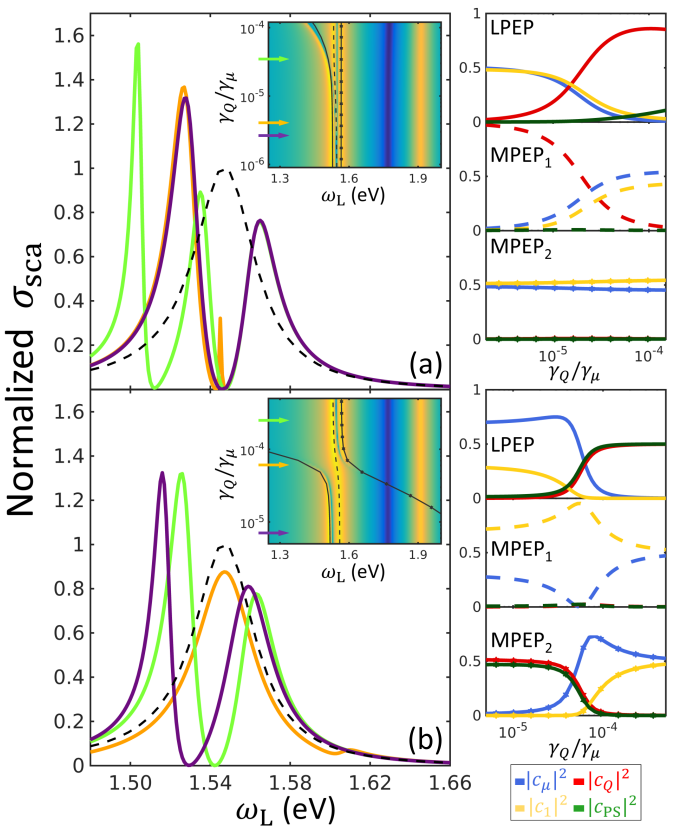

FIG. 4. Scattering spectra at the lowest plasmon resonance for the hybrid the QE-NPoM systems in Figure 3: $\omega_\mu = \omega_Q = \omega_1 = 1.55$ eV (a) and $\omega_\mu = \omega_1 = 1.55$ eV, $\omega_Q = \omega_{PS} = 2.40$ eV (b). Black dashed lines render σ_{abs} for the bare NPoM, and color solid lines correspond to hybrid systems with different quadrupole momenta. The insets show the cross section as a function of the laser frequency and γ_Q/γ_μ (arrows indicate the configurations in the main panels). Solid, dashed and connected-dotted lines render the PEP dispersion bands. Right panels plot the Hopfield coefficients for all cases as a function of γ_Q/γ_μ.

rotating frame. Using perturbation theory on the parameter E_L [25], we obtain the steady-state wavefunction for the QE-SP system, $|\psi_{SS}\rangle$, and compute its cross section as $\sigma_{sca} = \langle\psi_{SS}|\hat{M}^\dagger\hat{M}|\psi_{SS}\rangle$ (note that taking advantage of the deeply subwavelength dimensions of the system, we can drop the near-to-far-field Green's function in our calculation of the scattering spectrum).

Figure 4 renders the scattering cross section for the two configurations considered in Figure 3. The spectral window is centered around ω_1, the frequency of the lowest SP supported by the NPoM and whose contribution to the far-field signal is the largest. In both panels, the bare SP spectra is plotted in black dashed line (see SM for a comparison against numerical solutions of Maxwell's Equations). Three different γ_Q/γ_μ ratios are considered: orange lines correspond to the Q-values in the main panels of Figure 3, whereas violet and green lines plot spectra for lower and higher quadrupole momenta, respectively. The insets display σ_{sca} versus laser frequency and γ_Q/γ_μ within a wider spectral frequency, ranging beyond the scattering peak at $\omega_{2,1}$. Note the presence of an invisibility dip [20] at 1.77 eV, which originates from superposition effects among the emission from different SPs.

The violet spectrum in Figure 4(a) shows the Rabi splitting of the bare NPoM scattering peak, an indication of the formation of PEPs in the system due to the strong coupling between the lowest SP and the QE dipolar exciton [4]. The fingerprint of the quadrupole exciton becomes apparent only at larger γ_Q/γ_μ, giving rise to a third peak in σ_{sca} at $\omega_L = \omega_1$ (orange line). This maximum grows and broadens, and its position red-shifts, as the quadrupole moment increases further (green line). The right panels in Figure 4(a) plot the Hopfield coefficients for the three PEPs behind these far-field signatures. They are obtained from the projection of $|\psi_{SS}\rangle$ in the bare exciton-plasmon basis (for simplicity, we have restricted the plasmonic Hilbert space to the lowest SP and the PS). Following an increasing frequency order, the PEPs are labelled as lower, middle 1 and middle 2. A fourth (upper) polariton emerges at ω_{PS}, not shown here. These panels show that the peak at ω_1 in Figure 4(a) develops when MPEP1 losses partially its light-forbidden excitonic character. This is in turn transferred to LPEP, whose associated peak becomes narrower. On the contrary, MPEP2 is barely affected in this process. Importantly, this modification in the usual Rabi splitting phenomenology takes place within the parametric region in which the Purcell effect in Figure 3(a) is reduced and the QE lifetime is longest.

Figure 4(b) reveals that the Rabi splitting profile is altered even at the lowest γ_Q/γ_μ in the second QE-SP configuration. This higher sensitivity to the quadrupole exciton is a consequence of the large enhancement that g_Q^{PS} experiences as the QE is displaced across the cavity gap, see Figure 2(a). Note that due to the large spectral detuning between ω_1 and ω_{PS}, the scattering dip is no longer at $\omega_L = \omega_1$. Remarkably, by increasing the quadrupole moment, the lowest frequency peak vanishes, and the spectrum for the hybrid system resembles very much the one of the bare NPoM (orange line). This profile can be observed only within a narrow range of Q-values, beyond which a symmetric Rabi splitting spectrum, very similar to the one observed at $Q = 0$ is recovered (green line). The contourplot in the inset and the Hopfield coefficients shed light into this evolution of σ_{sca}. In this case, MPEP2, which initially originates from the strong coupling between the quadrupole exciton and the PS, becomes strongly Rabi-shifted towards ω_1. For large enough Q, anti-crossing among PEP bands takes place. As a result, LPEP and MPEP2 lose their content on the lowest SP mode, which in turn is transferred to MPEP1. In these conditions, light-allowed and light-forbidden QE states interact only through the PS and become completely dark. The Rabi splitting in σ_{sca} vanishes but, as shown in Figure 3(b), the large excitonic couplings to the PS lead to a fast oscilla-

tions in the QE population and an effective shortening of its lifetime.

To conclude, we have investigated the influence of light-forbidden excitons in plasmon-emitter coupling at the gap of nanoparticle-on-a-mirror cavity. We have developed a fully analytical description of the spectral densities for both dipolar and quadrupolar (dipole-inactive) transitions, obtaining the plasmonic natural frequencies and decay rates, as well as the different sets of plasmon-exciton coupling strengths. Using our approach, we have explored the near-field population dynamics and far-field scattering spectrum of these hybrid systems, revealing the conditions in which the quadrupole excitons lead to strong modifications in the Purcell effect and Rabi splitting phenomenology. Our results prove that, by means of surface plasmons, the internal degrees of freedom of microscopic light sources can be exploited for the realization of richer and more versatile platforms for polaritonic applications.

The authors thank Elena del Valle and Alejandro González-Tudela for fruitful discussions. This work has been funded by the Spanish MINECO under contracts FIS2015-64951-R, MDM-2014-0377-16-4 and through the "María de Maeztu" programme for Units of Excellence in R&D (MDM-2014-0377), as well as the EU Seventh Framework Programme under Grant Agreement FP7-PEOPLE-2013-CIG-630996.

* a.fernandez-dominguez@uam.es

[1] L. Novotny and N. van Hulst, Nat. Photonics **5**, 83 (2011).
[2] V. Giannini, A. I. Fernández-Domínguez, S. C. Heck, and S. A. Maier, Chem. Rev. **111**, 3888 (2011).
[3] G. Zengin, M. Wersäll, S. Nilsson, T. J. Antosiewicz, M. Käll, and T. Shegai, Phys. Rev. Lett. **114**, 157401 (2015).
[4] R. Chikkaraddy, B. de Nijs, F. Benz, S. J. Barrow, O. A. Scherman, E. Rosta, A. Demetriadou, P. Fox, O. Hess, and J. J. Baumberg, Nature **535**, 127 (2016).
[5] M. Ramezani, A. Halpin, A. I Fernández-Domínguez, J. Feist, S. R.-K. Rodríguez, F. J. García-Vidal, and J. Gómez-Rivas, Optica **4**, 31 (2017).
[6] E. Orgiu, J. George, J. A. Hutchison, E. Devaux, J. F. Dayen, B. Doudin, F. Stellacci, C. Genet, J. Schachenmayer, C. Genes, G. Pupillo, P. Samorì, and T. W. Ebbesen, Nat. Materials **14**, 1123 (2015).
[7] M. L. Andersen, S. Stobbe, A. S. Sorensen and P. Lodahl, Nat. Physics **7**, 215 (2010).
[8] F. Benz, M. K. Schmidt, A. Dreismann, R. Chikkaraddy, Y. Zhang, A. Demetriadou, C. Carnegie, H. Ohadi, B. de Nijs, R. Esteban, J. Aizpurua, J. J. Baumberg, Science **354** 726 (2016).
[9] P. Törmä and W. L. Barnes, Rep. Prog. Phys. **78**, 013901 (2015).
[10] H. T. Dung, L. Knöll, and D.-G. Welsch, Phys. Rev. A **57**, 3931 (1998).
[11] J. Galego, F. J. García-Vidal, and J. Feist, Phys. Rev. X **5**, 041022 (2015).
[12] P. Lodahl, S. Mahmoodian, S. Stobbe, A. Rauschenbeutel, P. Schneeweiss, J. Volz, H. Pichler and P. Zoller, Nat. Materials **541**, 473 (2017).
[13] M. Klessinger and J. Michl, *Excited States and Photochemistry of Organic Molecules* (VCH Publishers, New York, 1995).
[14] N. Rivera, I. Kaminer, B. Zhen, J. D. Joannopoulos, M. Soljacic, Science **353**, 263 (2016).
[15] J. R. Zurita-Sánchez and L. Novotny , J. Opt. Soc. Am. B **19**, 1355 (2002).
[16] R. Filter, S. Mühlig, T. Eichelkraut, C. Rockstuhl, and F. Lederer, Phys. Rev. B **86**, 035404 (2012).
[17] A. Alabastri, X. Yang, A. Manjavacas, H. O. Everitt, and P. Nordlander, ACS Nano **10**, 4835 (2016).
[18] J. B. Pendry, A. Aubry, D. R. Smith, and S. A. Maier, Science **337**, 549 (2012).
[19] R.-Q. Li, D. Hernangómez-Pérez, F. J. García-Vidal and A. I. Fernández-Domínguez, Phys. Rev. Lett. **117**, 107401 (2016).
[20] A. Aubry, D. Y. Lei, S. A. Maier, and J. B. Pendry, ACS Nano **5**, 3293 (2011).
[21] A. Demetriadou, J. M. Hamm, Y. Luo, J. B. Pendry, J. J. Baumberg, and O. Hess, ACS Phot. **4**, 2410 (2017).
[22] R. E. Raab and O. L. de Lange *Multiple Theory in Electromagnetism* (Claredon Press, Oxford, 2005).
[23] E.Waks and D. Sridharan, Phys. Rev. A **82**, 043845 (2010).
[24] P. M. Visser and G. Nienhuis, Phys. Rev. A **52**, 4727 (1995).
[25] R. Sáez-Blázquez, J. Feist, A. I. Fernández-Domínguez, and F. J. García-Vidal, Optica **4**, 1363 (2017).